PAPER

Check for updates

The relationship between microstructure and photocatalytic behavior in lanthanum-modified 2D TiO2 nanosheets upon annealing of a freeze-cast precursor†

Snejana Bakardjieva, [iD] *[a] Jakub Mares,[a] Radek Fajgar,[b] Victor Y. Zenou,[c] Michaela Maleckova,[d] Efthalia Chatzisymeon,[e] Hana Bibova[f] and Jaromir Jirkovsky[f]

Titanium dioxide modified with 3 wt% La was prepared *via* a green freeze-casting method, and its photocatalytic activity was tested in terms of its ability to degrade 4-chlorophenol (4-CP) and remove total organic carbon (TOC). Under annealing conditions, the freeze-cast precursor was transformed into an La-modified anatase with a well-defined 2D TiO2 nanosheet morphology. Rietveld refinement of the X-ray diffraction patterns confirmed the substitutional nature of the La cation that induced local structural variations and involved subtle ion displacement in the TiO2 lattice due to the ionic size effect. Despite nearly identical tetragonal structures, replacement of Ti with La alters the photocatalytic activity through a reduction in band gap energies and an increase in charge carrier mobility. Material annealed at 650 °C exhibited the highest photocatalytic performance and achieved efficient TOC removal. Upon annealing at 800 °C, nanoscale lanthanum-enriched regions were generated due to the diffusive migration of La cations and phase transition from anatase to rutile. The La^{3+} cation, acting as a structural promoter, supported 2D TiO2 growth with well controlled crystallite size, surface area and porosity. La^{3+} could be regarded as a potential electronic promoter that can reduce the band gap of 2D TiO2 nanosheets and can provide a signature of the electron transfer and carrier charge separation. Both methods, kinetics of degradation of 4-CP and TOC, provided similar results, revealing that the photocatalytic activity under UV light irradiation increased in the order 950C < 500 °C < 800 °C < 650 °C < TiO2-P25.

1 Introduction

The natural environment is a priceless part of our heritage. A healthy natural environment is vitally important for all ecosystems, and it is our responsibility to protect it. Water and air pollution are considered major environmental issues that should be urgently addressed. Organic compounds such as chlorophenols, are used as pesticides, herbicides and

[a]*Institute of Inorganic Chemistry of the Czech Academy of Sciences, 250 68 Husinec-Řež, Czech Republic. E-mail: snejana@iic.cas.cz*

[b]*Institute of Chemical Process and Fundamentals of the Czech Academy of Sciences, Rozvojova 2/135, 165 02 Prague, Czech Republic*

[c]*Nuclear Research Center-Negev, Department of Material Engineering, 841 90 Beer Sheva, Israel*

[d]*Charles University, Faculty of Science, Hlavova 2030/8, 128 42, Prague, Czech Republic*

[e]*School of Engineering, Institute for Infrastructure and Environment, The University of Edinburgh, Edinburgh, EH9 3JL, UK*

[f]*J. Heyrovsky Institute of Physical Chemistry of the Czech Academy of Sciences, Dolejskova 2155/3, 182 23 Prague, Czech Republic*

† Electronic supplementary information (ESI) available. See DOI: 10.1039/c9ra03940f

disinfectants, and they are considered priority environmental pollutants.[1] Over the past years, various aspects of photocatalysis have been reviewed, and the importance of this technology for the remediation of air and water pollutants is well documented.[2] Among several semiconductors, TiO2 has been proven to be one of the most widely used photocatalysts for decomposing organic compounds due to its strong redox ability, chemical and thermal stability and low cost.[3–5] Photocatalysts based on d[0] (Ti) transition metal oxides have emerged as good materials for heterogeneous photocatalytic systems, mainly because of their advantageous electronic configurations of empty d orbitals that minimize trapping of excited electrons and holes. Additionally, TiO2 is not classified as hazardous according to the United Nations' Globally Harmonized System of Classification and Labeling of Chemicals (UN-GHS 2011).[6] However, TiO2 has a certain drawback regarding its application under solar light. Due to the wide band gap of TiO2 (*i.e.*, 3.2 eV for anatase and 3.0 eV for rutile), only ultraviolet (UV) light can excite TiO2 to generate photoinduced holes (h[+]) and electrons (e[−]). Some of the strategies employed to increase the solar photoactivity of TiO2 include the addition of a cocatalyst (Pt,

RuO_2) as well as the doping of TiO_2 with nonmetal and metal ions to induce morphological changes.[7–9] These strategies have led to the discovery of using the lanthanide series of elements as the dopants because they have an effect on the stabilization of the anatase phase of TiO_2. Recent studies of Liu[10] and Cunha[11] reported the utilization of La_2O_3 as a booster for the heterogeneous photocatalytic degradation of ammonia and methane gases, respectively. The boosting effects of lanthanum on the degradation reaction could be attributed to several reasons. The most important phenomena involved in this mechanism are the stabilization of the active sites onto the TiO_2 surface in their stable $Ti^{(IV)}$ valence state[12] and the synergistic effect between La-involved active sites and Ti active sites due to direct contact between La cations and the TiO_2 matrix.[13]

La-modified TiO_2 photocatalysts are usually prepared by sol–gel processes,[14–17] which have their own drawbacks that include the requirement for expensive metal alkoxides, little control over the porosity due to shrinkage of a wet gel upon drying and slow rate of the solvent removal.[18] There is scientific and technological interest worldwide in developing cleaner and more efficient methods for the synthesis of catalysts with well-controlled morphology (size, shape and crystal structure). Therefore, great emphasis is currently placed on the implementation of environmentally friendly ("green") procedures that could reduce or even avoid the use and generation of hazardous substances while minimizing waste production, energy and time consumption.

Recently, ice nucleation and crystal growths have been used to create porous materials with controlled pore dimensions. This process has been termed "freeze-cast forming" (lyophilization) and uses ice formation to create microscopic ice voids in a solid body. Subsequent removal of the ice through sublimation (simple transition of substances from solid to vapor state, performed at low temperature and vacuum) leaves behind a rigid, porous material.[19] To date, little effort has been made on the growth of porous 2D TiO_2 nanosheets, which might be attributed to the limited use of the freeze-casting method in nanomaterials science, particularly in photochemistry and photocatalysis.[20–22] Herein, we use the freeze-cast technique suited for the synthesis of the series of nanocrystalline 2D TiO_2 materials from a thermally annealed freeze-cast peroxo-polytitanic acid (PPTA) precursor modified with 3 wt% La, and we drew connections between crystallographic structure and photoactivity. The technique uses little other than water, which is an environmentally friendly, nontoxic dispersing medium and costs very little as a tool, and is a huge saving compared to the sol–gel method. In addition, this method could be applicable to photocatalysts of all kinds. Among all rare Earth-modified TiO_2, the system based on the La^{3+} ion is of interest because its coordination improved the trapping-to-recombination rate ratio of photogenerated electrons and holes compared with pristine TiO_2.[23] We exploited the TiO_6 octahedral unit modulated by substitutionally incorporated La^{3+} to understand the influence of lattice distortion on the structural, optical, and electronic properties of 2D TiO_2 nanosheets. A set of the 4-CP photocatalytic degradation tests was carried out in an aqueous suspension under UV light

irradiation, and total organic carbon (TOC) removal (mineralization of 4-CP) was investigated simultaneously. Characterization results were compared to standard Degussa TiO_2-P25 to validate the advantages of the materials as obtained. In this research, several characterization techniques like X-ray powder diffraction (XRD), high-resolution transmission electron microscopy (HRTEM), X-ray photoelectron spectroscopy (XPS), Raman, FTIR, EPR and BET/BJH were used, resulting in aspects like detailed crystal structures and refinement of lattice distortions clarifying the effect of La^{3+} ions on the microstructure, charge carrier separation and photocatalytic efficiency of 2D TiO_2 nanosheets.

2 Experimental

2.1 Materials

Titanium(IV) oxysulfate (titanyl sulfate, $TiOSO_4$, Sigma-Aldrich spol. s.r.o., Prague, Czech Republic) was used as a TiO_2 precursor. Lanthanum(III) nitrate hexahydrate, $La(NO_3)_3 \cdot 6H_2O$ Assay Spec. ≥99%, served as the La dopant source. During material synthesis, an aqueous solution of ammonia (NH_3, solution purum p.a., 25–29%, Fisher Scientific, spol. s.r.o., Pardubice Czech Republic) was used for precipitation of the precursor and hydrogen peroxide (H_2O_2, solution purum p.a., 30%, Fisher Scientific, spol. s.r.o., Pardubice Czech Republic) for pH reduction. 4-Chlorophenol (4-CP, purity ≥ 99.9%, Sigma-Aldrich, Prague, Czech Republic) and AEROXIDE TiO_2-P25 (Evonik, Prague, Czech Republic) were used for the photocatalytic experiments.

2.2 Synthesis of La-doped TiO_2

La-modified TiO_2 nanosheets were prepared by a freeze-casting method[24–27] using aqueous colloids of peroxo-polytitanic acid (PPTA) and $La(NO_3)_3$ (see Scheme 1). In a typical experiment,

Scheme 1 Synthetic route for the preparation of [La(III)-peroxo-polytitanic Ti(IV)] precursor Ti_La_LYO.

4.80 g of titanyl sulfate was dissolved in 150 mL of distilled water at 35 °C (step 1). Then, 0.9 mL of La(NO$_3$)$_3$ solution was added (step 2), yielding a calculated value of 3 wt% of lanthanum to give a colorless solution. This solution was cooled for approximately 1 h in the freezer, and thereafter the precipitation was carried out at ~0 °C in aqueous ammonia until the pH reached 8 (step 3). The precipitate was filtered and washed several times to remove sulfate anions formed during the reaction. The precipitate as obtained was transferred into a beaker and re-suspended into 350 mL of distilled water. The pH of the resulting suspension was reduced by adding 20 mL of 30% hydrogen peroxide (H$_2$O$_2$), and it was stirred at ambient temperature until the solution turned from turbid yellowish to transparent yellow (step 4). The PPTA solution was added dropwise into Petri dishes immersed in liquid nitrogen (LN$_2$) (step 5). Frozen droplets were immediately freeze-dried at 10 mTorr, at −64 °C for 48 h by using VirTis Benchtop K, Core Palmer UK lyophilizer (step 6). After freeze-casting, a yellowish "granule-like" lyophilized precursor (lyophilized cake) was isolated (step 7).[23,25] The lyophilized precursor labeled Ti_La_LYO was further heat-treated under air at 500, 650, 800 and 950 °C for 1 h in each case (with rate 3 °C min^{-1}), and four new samples denoted as Ti_La_500, Ti_La_650, Ti_La_800 and Ti_La_950 were obtained (Scheme 1).

2.3 Characterization methods

X-ray powder diffraction patterns were collected using a PANalytical X'Pert PRO diffractometer equipped with a conventional X-ray tube (Cu$_{K\alpha}$ 40 kV, 30 mA, line focus) in transmission mode. An elliptic focusing mirror, a divergence slit 0.5°, an anti-scatter slit 0.5° and a Soller slit of 0.02 rad were used in the primary beam. A fast-linear position sensitive detector PIXcel with an anti-scatter shield and a Soller slit of 0.02 rad were used in the diffracted beam. Four XRD patterns were collected for each sample, in 2 theta range of 18–88° with step of 0.013° and 100 s per step dwelling time. Qualitative analysis of the XRD data was performed with the HighScorePlus software package (PANalytical, the Netherlands, version 3.0e), the DiffracPlus software package (Bruker AXS, Germany, version 8.0) and the JCPDS PDF database (JCPDS 2015).[28] For quantitative phase analysis we used GSAS-II.[29] This program permits to estimate the weight fractions of crystalline phases by means of the Rietveld refinement method. The estimation of the size of crystallites was performed on the basis of the Scherrer formula,[30] as implemented within the GSAS-II software, using all XRD reflections for each of the 4 patterns per specimen. For crystallite size evaluation, the machine broadening was estimated by analysis of NIST SRM 660a (LaB$_6$). Additionally, we applied electron crystallography *via* CrystalMaker™ 10.2 software[31] in order to investigate the crystal structure and point defects of nanoscale particles that cannot be studied by X-ray powder diffraction analysis. The morphology of the powdered samples placed on a carbon tape was investigated using Philips XL30CP scanning electron microscope (SEM). The measurements were carried out in a low vacuum mode (with secondary electrons detector) at accelerating voltage of 30 kV. The samples were observed without any coating in order to study their original texture. Transmission electron microscopy (TEM) was

carried out on a JEOL JEM 3010 microscope operated at 300 kV (LaB$_6$ cathode, point resolution 1.7 Å) and equipped with an EDS spectrometer. The images were recorded on a Gatan CCD camera with resolution of 1024 × 1024 pixels. Digital Micrograph and INCA software packages were used for structural and chemical analyses, respectively. Electron diffraction patterns were evaluated using the Process Diffraction program.[32] X-ray photoelectron spectra (XPS) were measured by Kratos ESCA 3400 furnished with a polychromatic magnesium X-ray source (Mg Kα radiation, energy 1253.4 eV). The base pressure was kept at 5.0 10^{-7} Pa. The spectra were fitted using a Gaussian–Lorentzian line shape and the Shirley background was subtracted. Survey spectra between 0–1000 eV were collected with incremental step size 0.2 eV and more detailed narrow spectra were taken over Ti 2p, La 3d, La 4d, O 1s and C 1s regions with the incremental steps 0.05 eV. The spectra were collected at constant pass energy 25 eV, which corresponds to peak resolution 0.8 eV. The samples were not sputtered before measurements to preserve chemical states of the measured elements. Spectra were calibrated to C 1s line centered at 284.8 eV. Specific surface area was determined by the BET method[33] using a Quantachrome Nova 4200E instrument. Nitrogen adsorption was carried out at −196 °C. The pore size (diameter and volume) distributions were evaluated from the nitrogen desorption isotherm using the cylindrical pore model (BJH).[34] Before each measurement, the annealed samples were outgassed for approx. 20 h at 200 °C, lyophilized samples were outgassed for approx. 35 h at room temperature (RT). Fourier transform infrared spectroscopy (FTIR) in transmission arrangement was also used for sample characterization. Absorption spectra were acquired using Nicolet Nexus 670 FTIR spectrometer in the region of 400–4000 cm^{-1}. Approximately 1 mg of the sample and 300 mg of potassium bromide were ground in agate mortar. The mixture was pressed into pellet of approx. 10 mm diameter. Raman spectra were collected by a Nicolet Almega XR dispersive spectrometer equipped with Olympus BX-51 microscope. 256 exposures with resolution 2 cm^{-1} were taken using excitation wavelength 473 nm with energy 5 mW. The formation of hydroxyl radicals was investigated using the spin trapping technique with a Bruker E-540 electron paramagnetic resonance spectrometer (EPR). The stock aqueous suspension of La modified TiO$_2$ (mg mL^{-1}) was carefully homogenized in an ultrasonic bath (1 min) followed by the addition of a spin trap agent (0.2 M DMPO). The final suspensions were immediately transferred into a quartz flat cell (WG 808-Q, Wilmad-LabGlass, USA). The samples were irradiated directly in the EPR resonator at room temperature. A xenon lamp (300 W, Newport, USA) was used as an irradiation source and a Pyrex glass filter (GG 300, Newport, USA) was applied to eliminate radiation wavelengths below 300 nm.

2.4 Photocatalytic degradation of 4-CP

The prepared photocatalysts (0.15 g L^{-1}) were added in an aqueous 4-chlorophenol solution (4-CP, 1.0 × 10^{-4} mol L^{-1}). The reactant mixtures were irradiated under identical conditions in a photoreactor equipped with 10 lamps (Sylvania Blacklight 8 watt, $\lambda_{max} = 368$ nm, intensity 6.24 mW cm^{-2}). The volume of the reactant mixture was 175 mL. The photocatalytic activity of the samples was monitored by measuring the

Paper

concentration of 4-CP in water (HPLC, Agilent Technologies 1200 Series, column LiChrospher RP-18, 5 μm, mobile phase mixture of methanol and water, UV/Vis absorption detection) as well as the total organic carbon (TOC-LCPH, Shimadzu). The instrumental method employs the incineration of the sample at 680 °C, resulting in the formation of CO_2. Inorganic carbon presented as carbonate is transformed with 0.1% HCl to CO_2. Formed CO_2 was detected by implementing IR absorption spectroscopy. Water samples (20 mL) were taken periodically at 60, 120, and 240 min and after 29 h (1740 min) of irradiation.

The reaction rate of 4-CP reduction was fitted to the pseudo first-order kinetic model:

$$\ln\left(\frac{C}{C_0}\right) = -kt \tag{1}$$

where C and C_0 are the summed 4-CP concentrations at time (t) and $t = 0$, respectively, and k is the pseudo first-order kinetic rate constant.[35–37] The method of UV-Vis diffuse reflectance spectroscopy was employed to estimate band-gap energies of the prepared La-modified 2D TiO_2 nanosheets. Diffuse reflectance UV-Vis spectra were recorded in the diffuse reflectance mode (R) and transformed to a magnitude proportional to the extinction coefficient (K) through the Kubelka–Munk function, $F(R\alpha)$.[38] A PerkinElmer Lambda 35 spectrometer equipped with a Labsphere RSA-PE-20 integration sphere using $BaSO_4$ as a standard was used. The band-gap energy E_{bg} was calculated by the extrapolation of the linear part of equation $\lambda_{bg} = 1240/E_{bg}$ (eV).[39,40]

3 Results and discussion

3.1 X-ray powder diffraction (XRD)

The X-ray powder diffraction analysis and Rietveld refined outputs of XRD patterns were used for characterization of the microstructure and evaluation of the polymorphic anatase–rutile phase transition. The diffraction patterns given in Fig. 1 show the crystallite structure evolution of the freeze-cast (lyophilized) precursor (Ti_La_LYO) and its postsynthesis annealing products (Ti_La_500, Ti_La_650, Ti_La_800, Ti_La_950). The wide reflections at $2\theta = \sim 33$ and $\sim 43°$ correspond to Mylar foil, which was used as the sample holder.
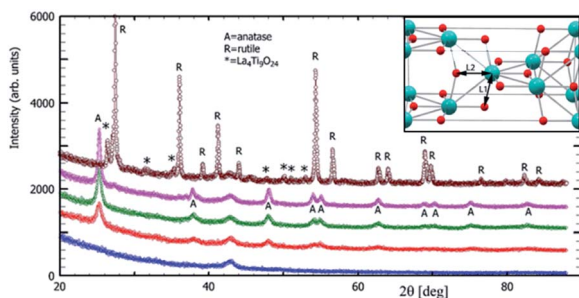

Fig. 1 X-ray diffraction patterns of the precursor Ti_La_LYO (blue line) and its postsynthesis annealing products Ti_La_500 (red line), Ti_La_650 (green line), Ti_La_800 (purple line), Ti_La_950 (brown line) and bond lengths projection by CrystalMaker software as inset.

The raw freeze-cast precursor Ti_La_LYO was identified as a strictly amorphous material (Fig. 1/blue curve). Annealing at 500 °C and 650 °C led to the formation of anatase phase only; the diffraction patterns in Fig. 1/red and green curves respectively correspond to tetragonal anatase (ICDD PDF 21-1272). The wide reflections at the sample Ti_La_500 were attributed mainly to its small crystallite size. At higher temperatures (i.e., 800 °C) reflections became narrower as the crystallites grew from 10(1) nm at 500 °C to 23(0) nm at 800 °C (Table 1). The volume of the anatase lattice grew from 135.96 Å^3 at 500 °C to 136.09 and 136.18 Å^3 after annealing at 650 and 800 °C, respectively (Table 2). Fig. 1/purple curve and Fig. 2a show the XRD pattern of sample Ti_La_800. It is evident that Ti_La_800 already contains a small fraction (7(1) wt%) of the rutile phase (ICDD PDF 21-1276).

Analysis of sample Ti_La_950 (Fig. 1/brown curve and Fig. 2b) shows that it contains mostly the rutile phase (86 wt%), but extra reflections belonging to $La_4Ti_9O_{24}$ oxide (ICDD PDF 36-0137) were also identified. The results in Table 1 established that the La cation stabilized the tetragonal anatase phase at temperatures up to 800 °C. Our results agree with previous observations.[41,42] According to the XRD data, the anatase crystallite size of the nonmodified 2D TiO_2 nanosheets prepared by the same synthetic route[27] increased from 26.1 nm to 101 nm while annealing from 500 to 800 °C, respectively. In this work, we report an increase in average crystallite size from 10(1) to 23(0) nm within the same temperature range (see Table 1), confirming that La cation inhibited grain growth as was also reported by Li et al.[42] The decrease in particle size compared to nonmodified 2D TiO_2 materials could be due to the segregation of La^{3+} at the grain boundaries that could hamper grain growth by restricting direct contact between adjacent TiO_2 grains.[43] Table 2 shows calculated lattice parameters, bond lengths and lattice volumes. The results indicated lattice expansion due to the possibility of La^{3+} cations with larger ionic radius ($r_{La} = 0.1016$ nm) to replace Ti^{4+} ions ($r_{Ti} = 0.068$ nm). We observed a linear decrease in the a-direction that is contrasted by the significant increase in the c-direction. Similar behavior among cell parameters using the La^{3+} or Nd^{3+} ion as a dopants has been reported in the literature.[44–48] The lack of complete experimental research about the local environmental coordination of the La^{3+} in the host TiO_2 lattice is one of the sources that resulted in many contradictory statements concerning substitutional vs. interstitial position of La cation. Many researchers believed that it was difficult for La cation to replace Ti ion in the lattice of anatase because of the mismatch[49] of the ionic radii. However, the ionic radius of La cation is still smaller than the ionic radius of oxygen ($r_{O_2} = 0.132$ nm), and addition of La cation may change the octahedral array in the anatase lattice. Our results from the Rietveld refinement revealed that the properties of 2D TiO_2 nanosheets modified with 3 wt% La could be dictated by the specific synthetic conditions, shedding light on observed microstructural variations. In previous research, we found that the binuclear adducts were formed by mixing $TiOSO_4$ as the source of Ti^{4+} and H_2O_2 (Scheme 1).[25,27] These adducts contain the planar Ti–O–O–Ti grouping where the Ti atoms are bridged by μ-oxygen and two μ-peroxy groups (Fig. 3a). We believe that the special stability of Ti_2O_5 units might be due to the planar

Table 1 Microstructural characteristics of La-modified TiO_2 obtained by XRD analysis[a]
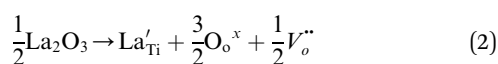
Sample	Phase composition	Anatase [wt%]	Rutile [wt%]	$La_4Ti_9O_{24}$ [wt%]	Anatase crystallite size [nm]	Rutile crystallite size [nm]	$La_4Ti_9O_{24}$ crystallite size [nm]
Ti_La_LYO	—	0	0	0	—	—	—
Ti_La_500	A[*]	100	0	0	10(1)	—	—
Ti_La_650	A	100	0	0	15(1)	—	—
Ti_La_800	A + R	93(1)	7(1)	0	23(0)	19(3)	—
Ti_La_950	R[**] + LTO[***]	0	86(1)	14(1)	—	88(2)	66(5)
TiO_2_P25	A + R	96.6	3.4		21.1	42.5	

[a] *A = anatase, **R = rutile, ***LTO = $La_4Ti_9O_{24}$.

structure of two five-membered rings[50] that are predicted to be free of strain (Fig. 3a).

The replacement of Ti^{4+} with La^{3+} in the binuclear peroxo-titanium adduct can lead to six fold coordination (with the same coordination number of 6 for both La^{3+} and Ti^{4+}) completed by linking of La^{3+} to O^{2-} ions in LaO_6 octahedrons (Fig. 3b). Even with six identical ligands, LaO_6 octahedrons could be highly deformed due to the larger ionic radius and the different distribution of the electrons of the La^{3+}. Additionally, it was proved that insertion of lanthanides altered the –O–Ti–O–Ti– atom arrangement by decreasing of the nonbridging oxygen (O^{2-}) during the phase transition from amorphous to polycrystalline anatase.[51] We found that the lengths of the axial Ti–O(L2) and equatorial Ti–O(L1) bonds increase by 0.5–0.8% compared to their counterparts in the pure anatase (TiO_2) host structure.[52] The Ti–O(L2) bond length increased its value up to 0.0061 nm, and the Ti–O(L1) bond length decreased its value up to 0.00013 nm (Fig. 1/inset and Table 2). Therefore, the generation of LaO_6 octahedron and the annealing process may cause structural deformations that adjust/alter chemical bond lengths in the TiO_2 unit cell.[47]

Substitution of La^{3+} cation into the Ti^{4+} site in the anatase TiO_2 structure led to the formation of an oxygen vacancy:

$$\frac{1}{2}La_2O_3 \rightarrow La'_{Ti} + \frac{3}{2}O_o^x + \frac{1}{2}V_o^{\bullet\bullet} \tag{2}$$

where Kröger–Vink notation[53] was employed to express the defects. La'_{Ti}, and $V_o^{\bullet\bullet}$ are the La^{3+} cation sitting on the Ti-lattice site and the oxygen vacancy $V_o^{\bullet\bullet}$, gives rise to high oxygen-ion mobility O_o^x.
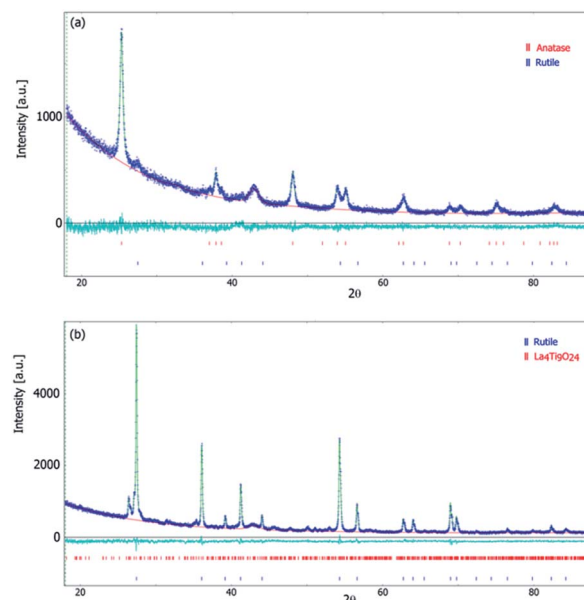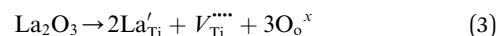

Fig. 2 Rietveld analyses using GSAS-II. (a) Ti_La_800, (b) Ti_La_950. Experimental data (dark blue '+' marks), fitted profile (green line), calculated background (red line) and difference between the calculated profile and the experimental data (blue line at the bottom). The position of the reflections is represented by vertical lines.

The imbalance in the charge created by La can also be compensated for:

$$La_2O_3 \rightarrow 2La'_{Ti} + V_{Ti}^{\bullet\bullet\bullet\bullet} + 3O_o^x \tag{3}$$

Table 2 Lattice parameters, bond lengths and lattice volume of La-modified TiO_2 obtained by XRD analysis

Sample	Anatase lattice parameters [Å]		Bond lengths [Å]	Lattice volume [Å³]	Rutile lattice parameters [Å]		$La_4Ti_9O_{24}$ lattice parameters [Å]		
	a	c			a	c	a	b	c
Ti_La_LYO	—	—	—	—	—	—	—	—	—
Ti_La_500	3.7890(1)	9.4700(2)	L1/1.9499 L2/1.9062	135.96	—	—	—	—	—
Ti_La_650	3.7884(2)	9.4821(9)	L1/1.9402 L2/1.9506	136.09	—	—	—	—	—
Ti_La_800	3.7858(2)	9.5019(5)	L1/1.9365 L2/1.9669	136.18	4.5880(2)	2.959(2)	—	—	—
Ti_La_950	—	—	—	—	4.5955(1)	2.9603(1)	14.147(1)	14.589(1)	35.511(3)

Fig. 3 Configuration of: (a) binuclear Ti_2O_5 adduct, and (b) binuclear La_2O_5 adduct.

(a) $Ti^{4+} + H_2O_2 \rightarrow Ti(O)_2(OH)_{n-2}^{4-n+} + {}_nH^+$

(b) $La^{3+} + H_2O_2 \rightarrow La(O)_2(OH)_{n-2}^{3-n+} + {}_nH^+$

where $V_{Ti}^{····}$ is a Ti cation vacancy at Ti site.

Sample Ti_La_950 shows large growth of 88(2) nm rutile nanocrystals NCs, which was more than four times bigger than the growth of anatase in the sample Ti_La_800. These results agree with Edelson[54] and Parker,[55] who proved that rutile can form particles of a much larger size than anatase due to the energy released during the polymorphic transition of meta-stable anatase to stable rutile TiO_2 phase. This energy is used for the sintering and faster growth of rutile NCs. The lattice parameters in the case of rutile phase (sample Ti_La_950) were not changed. Therefore, we can conclude that probably rutile cannot accommodate La^{3+} in its structure.

3.2 Morphology and microstructure of La-modified 2D TiO_2 nanosheets

Recently, we have published more insights regarding the capability of the freeze-casting procedure to produce TiO_2 nanomaterial with a layered structure.[24–27] Modification of the PPTA precursor by adding a noble metal (Ag and Au) or lanthanide element (Nd) does not change titania morphology and leads to a porous 2D TiO_2 structure identical to the structure of nonmodified TiO_2 samples.[56] SEM studies of the La-modified 2D TiO_2 nanosheets (i.e., Ti_La_500, Ti_La_650, Ti_La_800 and Ti_La_950) are in line with our previously published results. The morphology of the non-annealed precursor (Ti_La_LYO) is presented in Fig. 4a and b. We observed that the precursor obtained was predominantly amorphous in nature, since we could not recognize any grains with distinguishable shape and size (red dashed area in Fig. 4b). The result correlates well with the XRD pattern of Ti_La_LYO (see Fig. 1, blue curve). The amorphous state changed after heat treatment (Fig. 4c and d) and the joined crystalline lamellae, which is identifiable by shape and size, can be observed at temperatures up to 800 °C (Fig. 4e). Such lamellar morphology is a result of the controlled nucleation during the freeze-casting process, which can affect the phase morphology and stability.[57] The crystallization takes place only in the 2D direction, and the lamellar structure (2D nanosheets) with different degrees of crystallinity is preserved. At 950 °C, the 2D nanosheet morphology partly collapsed since the anatase–rutile transformation took place (Fig. 4f).

High resolution transmission electron microscopy (HRTEM) was used to study surface morphology, grain size distribution and lattice changes of samples Ti_La_500, Ti_La_650, Ti_La_800 and Ti_La_950. The TEM image of the Ti_La_LYO precursor taken at low magnification (Fig. 5a) shows high contrast, thus depicting a material with layered morphology. A high resolution TEM image (taken from the red marked area in Fig. 5a), is shown in Fig. 5b and reveals the evolution of a "core–shell" structure that could be described as a small (Ti–La) bi-nuclear core (Fig. S1a–c†) enveloped in a thin amorphous shell with the thickness of approximately 10 nm. Detailed STEM analysis and elemental mapping deduced that the surface of as-formed bi-nuclear (Ti–La) core is modified by the presence of surface hydroxide and peroxo groups (Fig. S1d and e†). Therefore, we can conclude that as-observed unique amorphous shell is consisting of a great quantity of (–OH) and (–OOH) groups.
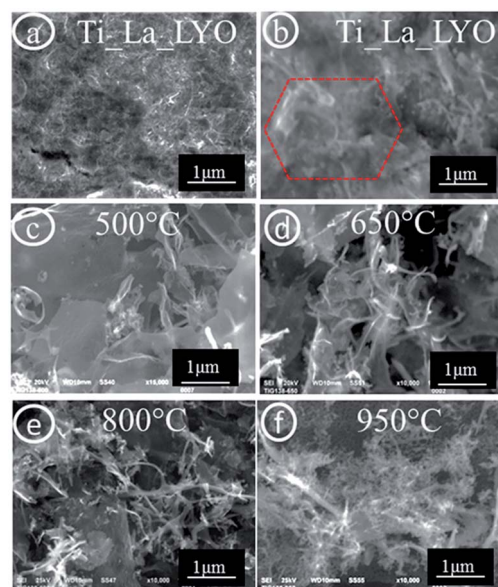

Fig. 4 SEM micrographs of: (a and b) Ti_La_LYO precursor and its post-annealed products, (c) Ti_La_500, (d) Ti_La_650, (e) Ti_La_800, and (f) Ti_La_950.
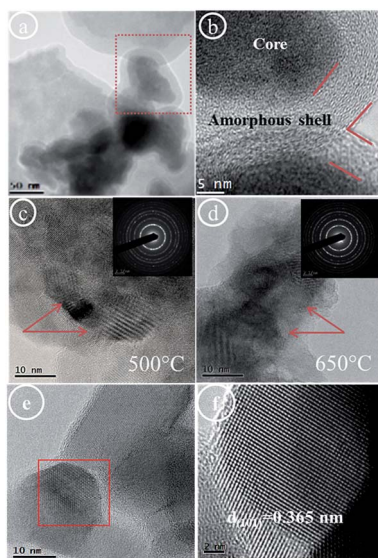
Fig. 5 HRTEM micrographs of: (a) Ti_La_LYO precursor (low magnification), (b) Ti_La_LYO precursor (high magnification), (c) Ti_La_500 and its FFT as inset, (d) Ti_La_650 and its FFT as inset. Red arrows show anatase grains, (e) high TEM magnification of selected area and (f) lattice fringes in HRTEM image of single NC.

The effect of freeze-cast process on morphology of Ti_La_LYO precursor was described in ESI (Fig. S1† and eqn (2) and (3)).

These results reveal that small amount of La (∼3 wt%) can play an important role as a nucleation agent by probably promoting the crystallization of TiO_2 as well as stabilizing covalent crosslinks in La-modified TiO_2 nanocrystals rather than in the case of the nonmodified TiO_2. The effect of temperature on the structural transformation of the lyophilized Ti_La_LYO precursor was also studied.

The HRTEM micrograph in Fig. 5c shows a high magnification TEM image of material Ti_La_500 obtained by annealing of the precursor at 500 °C. Layers are composed of closely packed NCs. The NCs were well dispersed, with an average size of 10 nm (marked with red arrows) and many different orientations that may exist between various crystallites in one polycrystalline aggregate. As the inset of Fig. 5c shows, the SAED pattern consists of series of concentric rings. The positions of diffraction rings match well with polycrystalline anatase TiO_2 (PDF ICDD 21-1272). The same result was also concluded from XRD characterization. Fig. 5d presents HRTEM results for Ti_La_650 material. Individual NCs with irregular shape and evaluated average size of 15 nm (marked with red arrows) were determined. The SAED pattern (inset graph of Fig. 5d) does not change at this temperature, thus confirming polycrystalline anatase TiO_2. The high-resolution TEM image of a single NC (taken from the red boxed area in Fig. 5e) presents lattice fringes, indicating interlayer spacing of $d_{(101)} = 0.365$ nm, which was found to be larger than the ones in standard TiO_2 (ICDD PDF 21-1272). The increase in the (101) interlayer spacing agrees with results derived from XRD analysis (see Table 1) and confirms the substitutional nature of La^{3+} ions at this temperature.

The HRTEM micrographs in Fig. 6(a and b) show the surface morphology of the sample Ti_La_800. In the micrograph taken at the lowest magnification, we observed a 2D agglomerate with incoherent structure consisting of fine intergrowth NCs with various shapes and sizes (Fig. 6a). The processing of the SAED analysis (Fig. 6b), from the black boxed area in Fig. 6a, reveals electron diffraction spots of anatase TiO_2 NCs (ICDD PDF 21-1272), (spots merged in yellow circles) and extra diffraction spots corresponding to hexagonal La_2O_3, (spots merged in green hexagon with indexed (10$\bar{2}$), (112), (10$\bar{3}$) and (20$\bar{2}$) planes belonging to the crystalline La_2O_3 with ICDD PDF 40-1279). The HRTEM/SAED results clearly indicate that the small nanosized domains of La_2O_3 can simultaneously grow along with anatase when annealed at a relatively high temperature (800 °C). Therefore, La^{3+} ions cannot be truly accommodated within the anatase lattice when the temperature is higher than 650 °C, which resulted in separation of Ti and La oxides.[58]

3.3 Surface properties of La-modified TiO_2 nanosheets

The results of specific surface area (BET) and porosity (BJH) of La-modified 2D TiO_2 nanosheets including the precursor Ti_La_LYO and samples annealed at 500, 650, 800 and 950 °C are shown in Table 3.

The specific surface areas of the pristine sample Ti_La_LYO and the sample annealed at 650 °C are large in comparison to the standard material TiO_2-P25. The surface area decreases with the synthesis temperature and reaches a maximum of 57 m^2 g^{-1} at 650 °C. Sample Ti_La_800 has a surface area like the area values obtained for TiO_2-P25. The surface area is decreased faster with increasing the temperature to 950 °C. The XRD analysis showed that the Ti_La_650 sample contains polycrystalline TiO_2 anatase with average crystallite size of ∼15 nm. The existence of small NCs corresponds well to the high specific area and is responsible for the stabilization of the mesoporous material with main pore radius of 4.4 nm (IUPAC 1972).[59] The following annealing up to 800 °C leads to a decrease in the specific surface area and pore volume, but the average pore size still remains in the mesoporous range. This stable mesoporous structure is preserved even at the annealing temperature of 950 °C, where the major phase is rutile. Addition of La improved the stability of pores even at high temperatures and could play
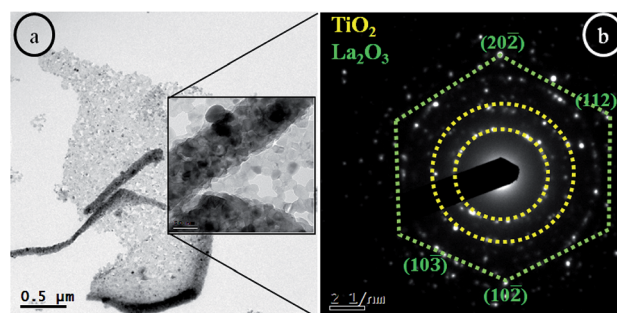

Fig. 6 TEM and SAED analysis of sample Ti_La_800: (a) low magnification TEM micrographs, (b) SAED analysis of black boxed area.

Table 3 BET, BJH, average pore size, band gaps and rate constants of La-modified 2D TiO_2

Sample	BET [$m^2 g^{-1}$]	BJH [$cm^3 g^{-1}$]	Average pore size [nm]	Band gap eV	Rate constant k [s^{-1}]
Ti_La_LYO	130	0.043	4.3	—	—
Ti_La_500	44	0.066	4.4	3.24	$(1.47 \pm 0.13) \times 10^{-5}$
Ti_La_650	57	0.052	4.4	3.19	$(2.67 \pm 0.36) \times 10^{-5}$
Ti_La_800	47	0.040	4.7	3.21	$(1.81 \pm 0.17) \times 10^{-5}$
Ti_La_950	26	0.018	4.5	3.13	$(1.38 \pm 1.63) \times 10^{-7}$
TiO_2_P25	50	—	—	3.10	$(5.84 \pm 0.26) \times 10^{-5}$

an important role by controlling nucleation during the freeze-casting process.[60,61]

The Fourier transform infrared (FTIR) spectra of La-modified TiO_2 samples are shown in Fig. 7. Measurements were carried out in the range of 400–4000 cm^{-1} (Fig. 7a). All spectra show broad bands between 3000–3800 cm^{-1}. These bands are centered at 3229 cm^{-1} and at 3417 cm^{-1}, and they are assigned to the stretching vibrations of O–H groups. The band observed at 1625 cm^{-1} corresponds to the deformation vibration of the adsorbed water. The bands located at 3229 and 1625 cm^{-1} decrease when the annealing temperature increases due to efficient desorption of surface water. The band at 1399 cm^{-1} is very intense for the lyophilized precursor (Ti_La_LYO), and it is typical for carbonates formed by naturally occurring CO_2 absorbed at the surfaces. During annealing, carbonates decompose, and the corresponding band becomes much weaker. The bands approximately 692 cm^{-1} and the pronounced peak at 903 cm^{-1} could be attributed to vibration modes of peroxo (–O–O–) group vibrations[62,63] (Fig. 7b). Both peaks disappeared after annealing due to the decomposition of the peroxo groups. The bands corresponding to O–Ti–O and Ti–O–Ti bonds are usually observed in the 800–400 cm^{-1} region (Fig. 7b), the former being observed at a higher wavenumber than the latter.[64] The lyophilized precursor Ti_La_LYO shows only Ti–O–Ti stretching vibration at 512 cm^{-1}. After heating to 500–800 °C, peroxo groups decompose, nonbinding oxygen is formed, and a broad vibration ν_{Ti-O} centered at approximately 800 cm^{-1} appears. The rutile form, prepared in this work at the highest temperature applied (950

°C), shows narrower ν_{Ti-O} and $\nu_{Ti-O-Ti}$ bands centered at 520 and 720 cm^{-1}, respectively (Fig. 7b). Presence of lanthanum oxide or hydroxide is not clear from the FTIR spectra due to the low atomic concentration of the La. However, La is believed to incorporate into titania even at low temperatures by the formation of Ti–O–La bonds.[65]

Raman characterization is in line with the XRD and the TEM observations and confirmed again that the precursor Ti_La_LYO is completely amorphous (Fig. 8). After annealing at 500–800 °C, the anatase TiO_2 form in the samples is shown by typical bands centered between 142 and 639 cm^{-1}. The FWHM of the E_g band centered at approximately 142 cm^{-1} is dependent on the size of the crystallites, and this parameter is 29, 25 and 24 cm^{-1} for the Ti_La_500, Ti_La_650 and Ti_La_800 samples, respectively, which confirms the increased crystallite size of samples annealed at elevated temperatures. At the highest temperature (950 °C) studied, the spectrum shows the presence of rutile (609 cm^{-1}/A_{1g}, 446 cm^{-1}/E_g for rutile) as the single crystalline form of TiO_2 in accordance with XRD results (see Table 1). The anatase form is not present, not even in traces, due to the much stronger cross-section of the anatase compared to the rutile form at excitation by a visible laser beam. Similar samples of nonmodified TiO_2 that are prepared by a similar procedure afford the formation of anatase-rutile mixtures forms even at 950 °C.

XPS characterization was employed to determine the composition and the chemical state of surface constituents at the surface region (~5 nm) for the La-modified 2D TiO_2 nanosheets. The Ti 2p region shows that all samples are formed by
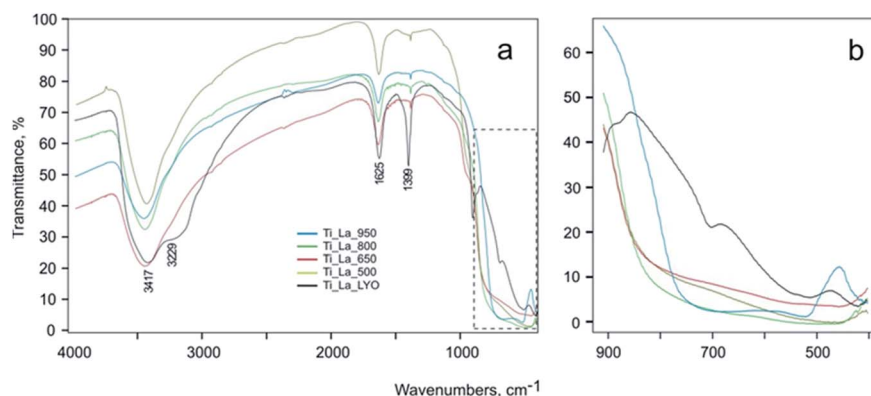

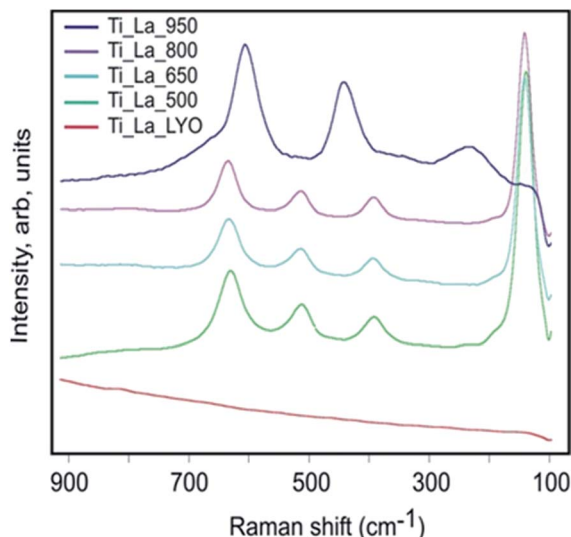**Fig. 7** (a) The survey IR spectra of the La-modified TiO_2 samples, and (b) the detailed spectra of the 400−900 cm^{-1} region.

Fig. 8 Raman spectra of the La-modified 2D TiO_2 nanosheets.

$Ti^{(IV+)}$ state.[66] Due to the amorphous character of the lyophilized precursor (Ti_La_LYO), the band Ti $2p_{3/2}$ is broader with FWHM at approximately 2.05 eV, while annealed samples became narrower because of the crystallization of titanium dioxide (see Fig. 9 and Table 4).

Lanthanum was measured in the 3d (820–870 eV) and 4d (85–115 eV) regions. This element has very well separated 3d spin–orbit components with further splitting. A magnitude of the multiple splitting (ΔE) was used for chemical state diagnosis of the lanthanum (Table 4). In the amorphous sample (Ti_La_LYO) and the samples annealed at 500–800 °C, the ΔE
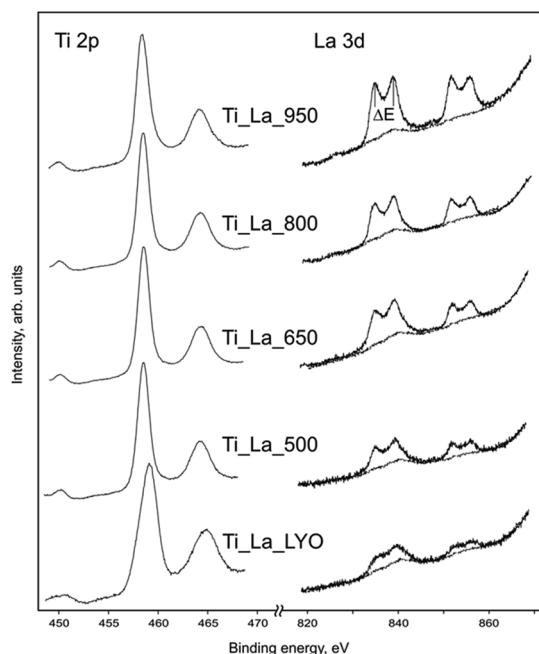
values fluctuate in the range of 4.1–4.2 eV, which indicates that lanthanum is predominantly in the form of hydroxide, while the rutile sample (Ti_La_950) with $\Delta E = 3.8$ eV contains mainly $La_2(CO_3)_2$. Elemental ratio of titanium/lanthanum was analyzed through Ti 2p/La 3d band areas and Ti 2p/La 4d band areas, and average Ti_xLa_y ratios were calculated (Table 4) using the characteristic response factors (7.9 for Ti 2p and 44.7 for La 3d bands). The areas were obtained after Shirley background subtraction. In the case of La $3d_{5/2}$ bands, Ti LMMa overlapping was also subtracted to obtain the representative lanthanum concentrations. The compositions prove variations in lanthanum concentration with heat treatment, indicating very high La cation mobility with increasing temperature (as measured by an energy-dispersive X-ray microanalysis method (EDS), which is discussed in Section 3.3.1).

3.3.1 Generation of nanoscale regions with different La concentration. In this section, we provide evidence founded upon the atomic scale observation showing nanoscale regions with different distributions of La cation.[67] The low magnification TEM image of sample Ti_La_800 is shown in Fig. 10a. The 2D agglomerate composed of closely packed crystals with the size of several tens to hundreds of nanometers can be observed. Elemental mapping providing in high resolution STEM/HAADF mode revealed the distributions of La element (Fig. S2†). The high magnification TEM micrograph (Fig. 10b) inferred a nanoscale region (we also called it contact region), where merged NCs are imaged. Based on HRTEM/SAED analysis, we can suggest that during the annealing at 800 °C, La cations are redistributed through the anatase lattice, and a new integrated 2D heterostructure can be drawn at high temperature.[68] The main factor affecting redistribution during heat treatment in air could be the diffusivity of the La cation. Substitutionally incorporated La^{3+} will escape from its lattice position through a vacancy mechanism due to the low formation energy of the $La'V_o^{\bullet\bullet}$ vacancy pair.[69] The migration of La^{3+} to the surface may be influenced by concomitant rearrangement of the Ti and oxygen atoms, since at this temperature, phase transition from anatase to rutile takes place (Table 1) and La_2O_3 in the form of an uppermost surface layer could be spontaneously separated. Our HRTEM/SAED and XPS results strongly support this hypothesis. The atomic scale observation of the interfacial structure (Fig. 10d) was fitted and visualized by CrystalMaker™ 10.2 software[31] based on the high resolution HRTEM image taken from the red boxed area in Fig. 10c. Two separate crystal lattice images indicate two single crystals belonging to TiO_2 (NC #1 from Fig. 10c) with [100] growth direction and La_2O_3 (NC #2 from Fig. 10c) with [010]

Fig. 9 XPS spectra of La-modified TiO_2 presented by Ti $2p_{3/2}$ and La $3d_{5/2}$ regions.

Table 4 XPS results for La modified TiO_2

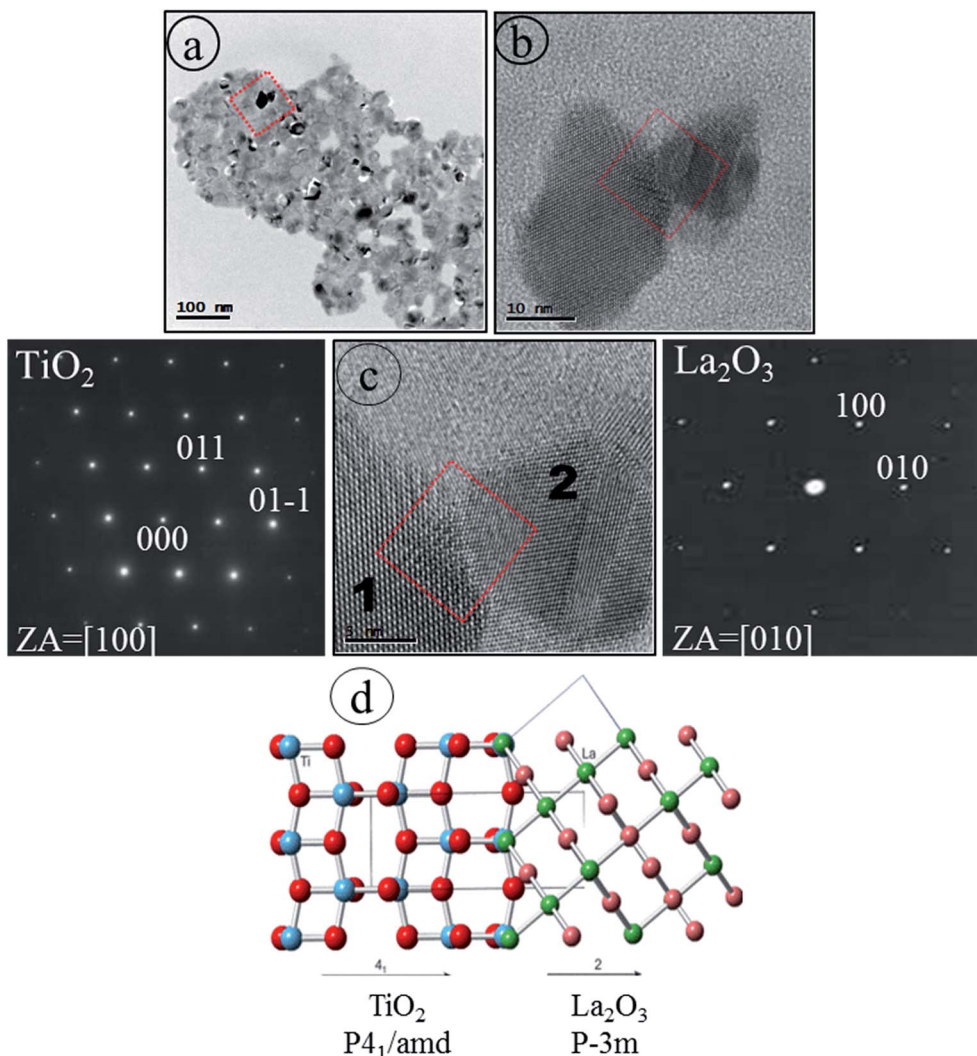| Sample	Ti $2p_{3/2}$ FWHM eV	ΔE/La $3d_{5/2}$ eV	Composition Ti_xLa_y
Ti_La_LYO	2.1	4.1	$Ti_{1.00}La_{0.07}$
Ti_La_500	1.4	4.2	$Ti_{1.00}La_{0.10}$
Ti_La_650	1.3	4.1	$Ti_{1.00}La_{0.13}$
Ti_La_800	1.3	4.1	$Ti_{1.00}La_{0.17}$
Ti_La_950	1.5	3.8	$Ti_{1.00}La_{0.26}$

Fig. 10 HRTEM images of sample Ti_La_800 (a) at low magnification (b) HRTEM image showing two grains, (c) high HRTEM magnification of the contact region and SAED taken from grains #1 and #2, (d) schematic representation by CrystalMaker software illustrating integrated 2D structures.

growth direction. The charge imbalance and the formation of a Ti–O–La bond[70] may be predicted. Additionally, the La^{3+} ions could have a stabilizing effect on the Ti–O bond[67] because the more electropositive La^{3+} will drive its electronic density toward O^{2-} so that it can use this increased concentration of electrons to strengthen the bonding between the less electropositive Ti^{4+} ions. Our results confirm that electron crystallography *via* using electron diffraction patterns could provide an original way to solve the crystal structure and point defects in NCs that cannot be studied by XRD analysis.

To confirm that new nanoscale regions are generated, detailed HRTEM observations and EDS were conducted to localize the element lanthanum in the Ti_La_800 sample. Distinct NCs are well observable in the high resolution TEM image (Fig. 11a) taken from the selected region (see the inset in Fig. 11a). Even the EDS analysis shows the presence of O, Ti and La, the change of interface stoichiometry has then been detected. The EDS analysis (see Fig. 11b) reveals that La

concentrations (7.32 wt%) is higher at the uppermost surface region (yellow boxed area in Fig. 11a) in comparison with La concentrations (6.42 wt%) in the surface near this region (blue boxed area in Fig. 11a), indicating that the La enriched the uppermost surface region when the temperature was increased to 800 °C. Our HRTEM observations are in line with previous TEM studies of Kato *et al.*,[71] who showed that higher concentration of La at the edges and surface grooves was possibly responsible for the darker TEM contrast (see Fig. 10a).

3.4 Photocatalytic decomposition of 4-CP

HPLC and TOC measurements have been applied for better understanding the photocatalytic performance of the as-prepared La-modified 2D TiO_2 materials (photocatalysts). The results are shown in Fig. 12, where we observed that the highest 4-CP removal is obtained in the presence of Ti_La_650 followed by Ti_La_800, Ti_La_500 and Ti_La_950 photocatalysts. The
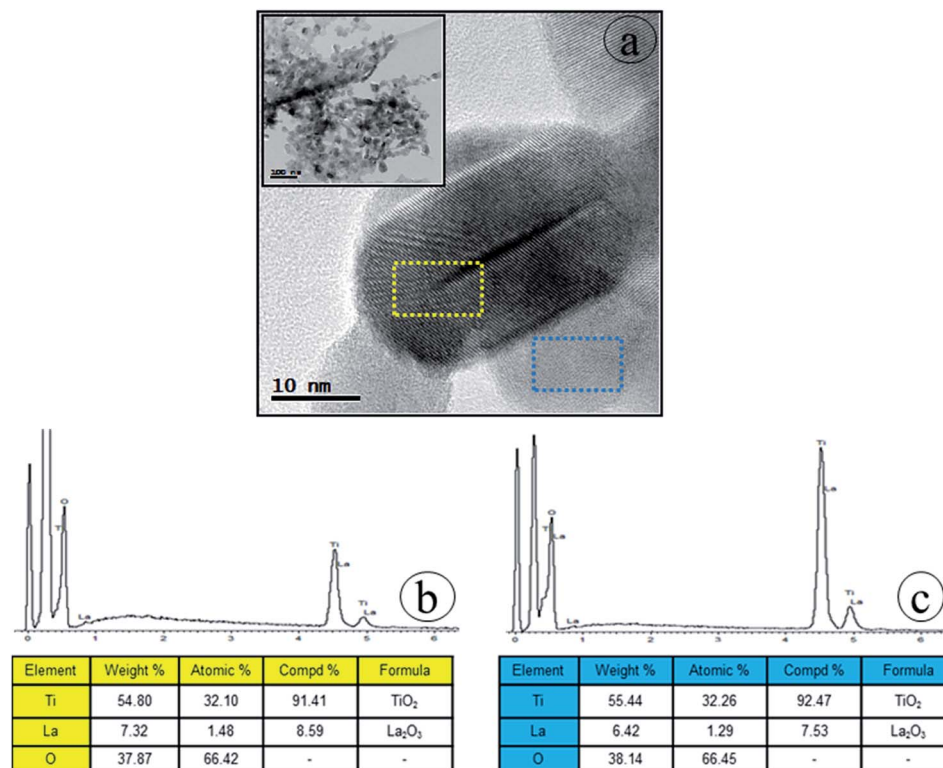
Element	Weight %	Atomic %	Compd %	Formula
Ti	54.80	32.10	91.41	TiO₂
La	7.32	1.48	8.59	La₂O₃
O	37.87	66.42	-	-

Element	Weight %	Atomic %	Compd %	Formula
Ti	55.44	32.26	92.47	TiO₂
La	6.42	1.29	7.53	La₂O₃
O	38.14	66.45	-	-

Fig. 11 (a) HRTEM micrograph of sample Ti_La_800 and EDS analysis of the (b) uppermost surface region (yellow boxed area) and (c) surface near region (blue boxed area).

degradation curves of 4-CP (Fig. S3†) under UV irradiation light showed similar results.

The calculated degradation rate constants k (s^{-1}) and band gap energies (E_g) are shown in Table 3. The obtained (E_g) values (Fig. S6†) are correlated with UV-Vis analysis (Fig. S4†) and Kubelka–Munk function (Fig. S5†).

For materials Ti_La_650 and Ti_La_800, the E_g value was below the reference anatase sample ($E_g = 3.24$ eV) and non-

Fig. 12 Photocatalytic degradation of 4-CP in the presence of Ti_La_500, Ti_La_650, Ti_La_800, Ti_La_950 and TiO₂-P25 catalysts.

modified 2D TiO₂ nanosheets obtained by the same method.[27] The best performance in 4-CP photocatalytic decomposition was achieved with Ti_La_650 material that has the lowest E_g and related redshift of the optical absorption. The higher photocatalytic efficiency of the Ti_La_650 catalyst can be explained by substitutional incorporation of La³⁺ into the anatase lattice, which has a clear positive effect on the photocatalytic activity under UV light irradiation. At this temperature, La³⁺ stabilized the anatase structure, decreased the size of the crystallites, increased surface area and exhibited distribution of pores predominantly in the mesoporous range (Table 1). We could accept that mesoporous Ti_La_650 material with a large surface area is the best photocatalyst, since a larger surface area offers more active adsorption sites. Further annealing at 800 °C leads to a decrease in the photocatalytic efficiency under UV light of Ti_La_800 material. The differences in the surface area and particle shape affect the redistribution of the La³⁺ on the Ti_La_800 material resulting in its lower photoefficiency. Annealing at the temperature of 950 °C resulted in a full conversion from anatase to rutile and a change in all microstructural characteristics and photocatalytic activity.

Mineralization of contaminants into the natural environment (for instance, 4-CP in wastewater) is very important for practical applications. Herein, we used the TOC removal as an inexpensive test to evaluate the La-modified 2D TiO₂ materials. The TOC removal with the time is illustrated in Fig. 13.

The mineralization of 4-CP in the presence of Ti_La_500, Ti_La_650, Ti_La_800 and Ti_La_950 photocatalysts is fast in the
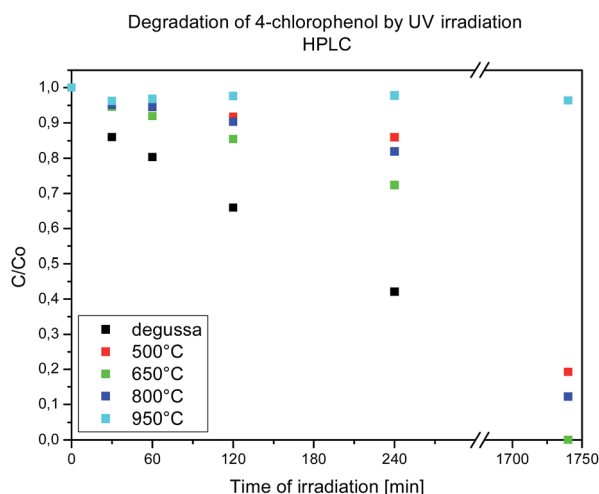
first 120 min of treatment but decreases thereafter. The highest TOC removal was achieved in the presence of Ti_La_650 with complete mineralization (100% TOC removal) taking place after 30 h of photocatalytic treatment. Mineralization of 4-CP over Ti_La_650 photocatalyst can be connected to the suppression of the electron–hole recombination by La^{3+} in the TiO_2 lattice and the creation of $HO^{\bullet}$ radicals by oxidation of holes. $HO^{\bullet}$ radicals could be the primary oxidizing species which breaks down 4-CP into a variety of intermediate products on the route to total mineralization to carbon dioxide.[72] As outlined above, the Ti_La_650 photocatalyst was found to be more efficient than other La-modified 2D TiO_2 photocatalysts in terms of 4-CP removal. La-modified 2D TiO_2 nanosheets obtained after annealing at 800, 500 and 950 °C required longer irradiation times for the complete mineralization of 4-CP. The main reason for such behavior could be that the formation of intermediates detected in the 4-CP oxidation pathway were ring compounds (hydroquinone, catechol, benzoquinone) breaking down to yield CO_2, and their next competition with separated La_2O_3 for active centers on the catalyst surface.[70] The formation of hydroxyl radical spin adducts by EPR spectroscopy (with DMPO)[73] was also employed to probe the nature of the reactive oxygen species generated on the surface of Ti_La_650 photocatalyst. As depicted in Fig. 14a, four characteristic peaks of DMPO-·OH were observed, and their intensities increased with irradiation time (Fig. 14b).

Results demonstrate that the Ti_La_650 catalyst shows a high production of hydroxyl radicals that greatly contribute to the degradation of 4-CP. This indicates that the $HO^{\bullet}$ are generated on the surface of Ti_La_650, and the illuminated photocatalyst provides a strong indication that this material can be efficiently excited by UV light to create mobile charge carriers (e^-/hole$^+$ pairs) and that the charge separation is maintained long enough to react with adsorbed H_2O and produce a series of active $HO^{\bullet}$ radicals that finally induce the decomposition of 4-CP.[74]

In addition, an experiment was performed in the presence of the TiO_2-P25 photocatalyst, under the same operating conditions, to establish a comparison against commercially available standard photocatalysts. Our results show that with TiO_2-P25, the decrease in 4-CP concentration was faster and the reduction rate of TOC was higher than with Ti_La_500, Ti_La_650, or Ti_La_800. The greater photoeffectiveness of the TiO_2-P25 could be due to various factors. TiO_2-P25 is known to be a mixture containing more than 80% anatase with a minor amount of rutile and a small amount of amorphous phase.[75] In spite of several presumptions such as synergistic effect, tightly interwoven structures of anatase and rutile NPs[76] or aggregation of particles by interparticle dehydration,[73] we can suggest that the higher activity of TiO_2-P25 in the degradation of 4-CP could be attributed to the active role of rutile NCs which can act as an electron sink hindering recombination in anatase NCs.[77]

Based on calculated (E_g) of the Ti_La_500, Ti_La_650, Ti_La_800 and Ti_La_950 samples, only the TiLa_950 material was tested as a photocatalyst using a simulated solar light (lamp Oriel LCS-100 simulated solar light). Due to presence of light in the UV region and higher intensity of the mercury lamp, the high photocatalytic activity is observed, showing complete degradation of the model compound (4-CP). HPLC analysis (Fig. S7†) was applied for better understanding the photocatalytic performance of sample Ti_La_950. The observed rate constant $k\,(s^{-1}) = 6.621 \times 10^{-5}$, demonstrated that the decrease in 4-CP concentration was faster and the reduction rate was higher than with Ti_La_500, Ti_La_650, or Ti_La_800 and even the TiO_2-P25. Our results show that the increase of temperature up to 950 °C and La doping resulted in structural transition from anatase to 86 wt% rutile TiO_2 and separation of a $La_4Ti_9O_{24}$ (14 wt%) (see Table 1). The $La_4Ti_9O_{24}$ consists of a complex network of octahedrally-coordinated titanium sharing corners and edges with each other and linked by two six coordinated and one eight coordinated lanthanum atom. The distortions of the TiO_6 coordination polyhedra in $La_4Ti_9O_{24}$ have been found to show some similarities to those seen in other titanate materials, even the orthorhombic crystal system of $La_4Ti_9O_{24}$ with lattice parameters $a = 14.1458$ Å, $b = 35.5267$ Å and $c = 14.5794$ Å. The most common representation between rutile TiO_2 and $La_4Ti_9O_{24}$ in the view of the electronic and optical properties could be the networks of $[TiO_6]$ octahedron building blocks[78] One can see that the crystallite domain size that can be achieved by La-modified 2D TiO_2 nanosheets, even after annealing up to 950 °C is still up to nanoscale range – 100 nm (see Table 1), assuming that the intermolecular charge hopping across grain boundaries could be very efficient. The improvement in charge carrier mobility could be due to the improved control of crystallization guaranteed charge hopping through ordered $Ti_{1-x}La_xO_{2-\delta}$ domains (McCulloch et al., 2006) in all annealed samples (Ti_La_500, Ti_La_650, Ti_La_800 and Ti_La_950).[79]

3.5 The effect of La^{3+} on the evolution of complex microstructure

As was demonstrated by XRD and Raman characterization, the bulk structure of La-modified 2D TiO_2 nanosheets consists of anatase structure up to 650 °C (Ti_La_650 sample). Surface analysis by XPS and HRTEM/SEAD/EDS reveals that the
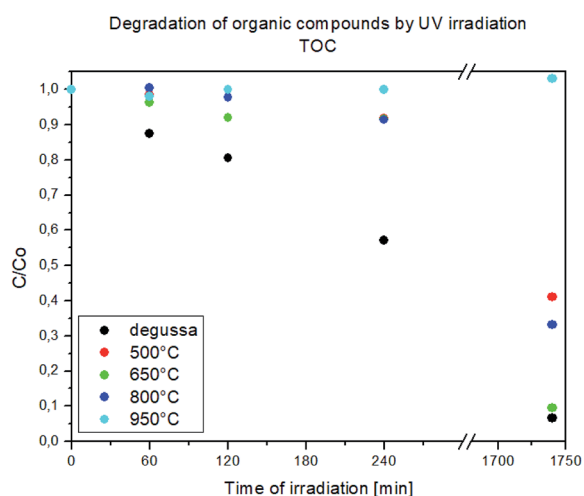

Fig. 13 TOC removal during the photocatalytic treatment of 4-CP in the presence of Ti_La_500, Ti_La_650, Ti_La_800, Ti_La_950 and TiO_2-P25 catalysts.
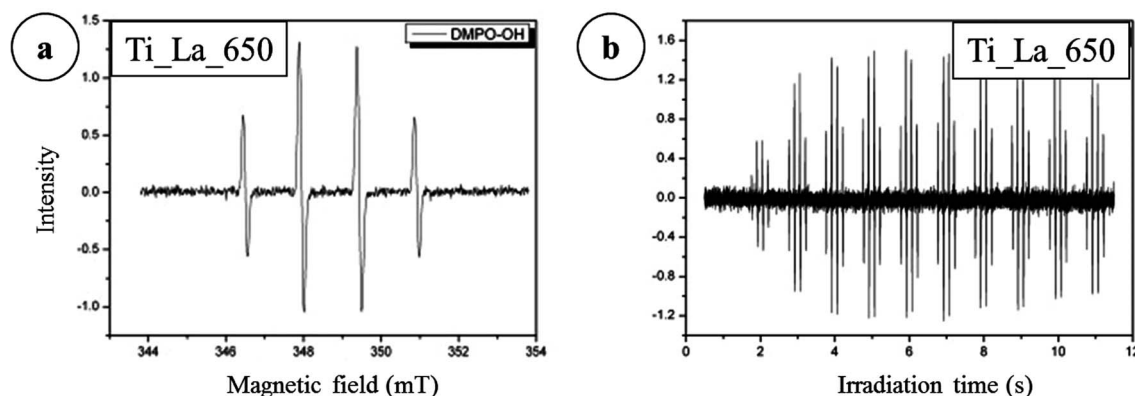
Fig. 14 EPR signal of the DMPO−HO˙ adducts in (a) the suspensions of sample Ti_La_650 (b) number of spectra after irradiation.

uppermost La_2O_3 surface layer is spontaneously separated at 800 °C (Ti_La_800 sample). Based on these findings, two models that led to the discovery of La^{3+} cation as a promoter of the reaction kinetic and the micro-texture of 2D TiO_2 nanosheets (photocatalysts) can be suggested.

3.5.1 La^{3+} as a kinetic promoter of the 4-CP photocatalytic degradation process. A great number of studies[14,15,17,80] have already reported that replacement of Ti^{4+} with La^{3+} leads to redshifted absorption. Our results are in line with this statement, since redshift of the absorption edge of Ti_La_650 and Ti_La_800 materials and narrowing of the band gap compared to the non-La-modified 2D TiO_2 materials were calculated. This redshift cannot be rationalized based on previous reports observing that with decreasing crystallite size the optical edge tended to shift to higher energy.[81] In the presented work, increasing the temperature leads to a linear increase in the crystallite size (Table 1). The primary effect of the La^{3+}, *i.e.*, charge separation of electrons and holes, could be influenced by differences in the La cation distribution. For a fixed (3 wt%) weight of lanthanum, many planar NCs are packed closely together in form of bigger agglomerates yielding greater diffusion distance of the charge carriers. Additionally, the grain boundaries observed by HRTEM could act as dislocation sources. We found that rate constant of Ti_La_650 equates with the highest rate of 4-CP degradation (Table 3) and believe that larger concentrations of La^{3+} in Ti^{4+} site could alter the energy for the interfacial charge transfer through a strong decrease of the carrier mobility. Our EPR observation of the Ti_La_650 material suggests that electrons may react with the dissolved oxygen to yield superoxide radical anions ($\cdot O_2^-$), which further react with H^+ and electrons to generate highly reactive hydroxyl radicals (HO˙) to enhance the photodegradation process. Small portions of oxygen vacancies ($V_O^{\cdot\cdot}$) may be trapped at the interfaces, but most of them can pile up along the surface to cause faster kinetic reaction, *i.e.*, 4-CP degradation. The extracted values of rate constants for non-La-modified 2D TiO_2 nanosheets[27] could suggest that anatase NCs smaller than ∼15 nm exhibit faster charge transfer kinetics. The oxidation and reduction reactions on La-modified 2D TiO_2 nanosheets appear to be selective, which extends their benefit.

3.5.2 La^{3+} as a promoter of the microtexture of 2D TiO_2 photocatalysts. In general, the band energy structure and consequently the photocatalytic efficiency can be influenced by the geometrical arrangement of constituent atoms. HRTEM findings suggest that in the contact nanoscale regions, NCs junctions could dominate the photocatalyst behavior rather than the intrinsic TiO_2 region. As we have shown (Fig. 6 and 10), a single La-modified 2D TiO_2 agglomerate is composed of closely packed planar NCs tending to form a two-dimensional network along a given crystallographic orientation. Furthermore, we observed that the photocatalytic behavior is likely to have temperature dependence, which is different from Ti_La_500, Ti_La_650, Ti_La_800, and Ti_La_950 materials. We assert that when La^{3+} is substitutionally incorporated into the TiO_2 lattice (Ti_La_650 photocatalyst), electron capture may involve diffusion across many NCs due to the 'antenna effect' expressed in transferring the photon energy between aggregated NCs with the same crystallographic orientation[82] (Fig. 15a).

As the annealing temperature was increased to 800 °C, two parallel-competitive reactions were starting: transition from metastable anatase to stable rutile and redistribution/escape of La^{3+} through the anatase lattice (Ti_La_800 sample). We observed significant variations in lattice parameters relative to the geometry and volume of the unit cells (Table 2) as well as changes in surface chemical composition (Table 4). We may suggest that is thermodynamically disfavored for rutile with smaller unit cell volume and higher density to accommodate La^{3+} with a larger ionic radius. As the temperature increases, La^{3+} cannot maintain the stable $[LaO_6]$ octahedral unit cell geometry, and it migrates towards the surface and forms the uppermost La_2O_3 layer (Fig. 15b). The Ti_La_800 material shows a wider band gap than Ti_La_650 and demonstrates a decay rate constant of 4-CP degradation. After La resides, a new $Ti_{1-x}La_x$-$O_{2-\delta}$ heterostructure with different bond lengths could be created, suggesting generation of partial occupied or unoccupied states in the band gap that would facilitate the formation of recombination centers.[83] Therefore, different conditions for transfer of electrons from the valence band to the conduction band could be achieved, leading to different photocatalytic performance of Ti_La_650 and Ti_La_800 photocatalysts.
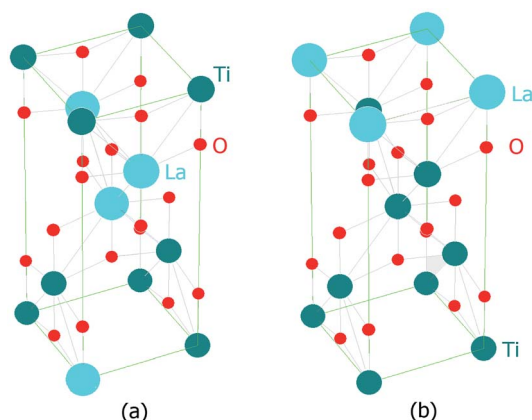
Fig. 15 Schematic representation by CrystalMaker software illustrating: (a) La cations randomly dispersed in the TiO_2 lattice (Ti_La_650 photocatalyst), and (b) La cations escaped from the anatase lattice and separated as the uppermost La_2O_3 surface layer (Ti_La_800 photocatalyst).

4 Conclusions

In this work, a freeze-casting method was developed by using PPTA as precursor to prepare La-modified 2D TiO_2 nanosheets. The surface and bulk properties of La modified 2D TiO_2 nanosheets obtained by annealing from 500 to 950 °C were investigated *via* surface (XPS, HRTEM) and bulk (XRD, Raman, UV-Vis) experimental techniques. Lattice distortions induced by replacement of Ti^{4+} with La^{3+} was observed at 650 °C. At higher temperatures, the diffusion mechanism led to the escape of La^{3+} from the anatase lattice, and the uppermost La_2O_3 surface layer was spontaneously separated. La^{3+} ion acted as a structural promoter, which stabilized smaller anatase TiO_2 NCs (from 10 to 23 nm) and increased the BET surface area (up to 57 m^2 g^{-1}). La^{3+} cation could be regarded as a potential electronic promoter that can reduce the band gap of 2D TiO_2 nanosheets and that can provide a signature of the electron transfer and carrier charge separation. The photocatalytic activity was determined by measuring the kinetics of degradation of 4-CP and TOC. Both methods provided similar results, establishing that the activity increased in the order 950 °C < 500 °C < 800 °C < 650 °C < TiO_2-P25 under UV light irradiation. Ti_La_950 material made from rutile and $La_4Ti_9O_{24}$ could be a promising candidate for a use as an efficient photocatalyst in degradation of 4-CP under simulated solar light.

Conflicts of interest

There are no conflicts to declare.

Acknowledgements

References

1 M. Pera-Titus, V. G. Molina, M. A. Baños, *et al.*, *Appl. Catal., B*, 2004, **47**, 219–256.

2 S. W. Verbruggen, *J. Photochem. Photobiol., C*, 2015, **24**, 64–82.

3 K. T. Ranjit, I. Willner, S. H. Bossmann and A. M. Braun, *J. Catal.*, 2001, **204**, 305–313.

4 Y. Jiang, H. Ning, Ch. Tian, B. J. Jiang, Q. Li, H. Yan, X. Zhang, J. Wang, L. Jing and H. Fu, *Appl. Catal., B*, 2018, **229**, 1–7.

5 S. Hu, S. Hu, P. Qiao, L. Zhang, B. J. Jiang, Y. Gao, F. Hou, B. Wu, Q. Li, Y. Jiang, Ch. Tian, W. Zhou, G. Tian and H. Fu, *Appl. Catal., B*, 2018, **239**, 317–323.

6 United Nation's, *Globally System of Classification and Labeling of Chemicals*, UN, New York and Geneva, 4th edn, 2011, ISBN no. 978-92-1-117042-9.

7 S. In, A. Orlov, F. Garcia, M. Tikhov, D. S. Wright and R. M. Lambert, *Chem. Commun.*, 2006, **40**, 4236–4238.

8 J. Lukáč, *et al.*, *Appl. Catal., B*, 2007, **74**, 83–91.

9 A. Kudo, H. Kato and I. Tsuji, *Chem. Lett.*, 2004, **33**, 1534–1539.

10 H. C. Liu, H. Wang, J. H. Shen, Y. Sun and Z. M. Liu, *Catal. Today*, 2008, **131**, 444–449.

11 A. F. Cunha, N. Mahata, J. M. Orfao and J. L. Figueiredo, *Energy Fuels*, 2009, **23**, 4047–4050.

12 R. Kam, C. Selomulya, R. Amal and J. Scott, *J. Catal.*, 2010, **273**(1), 73–81, DOI: 10.1016/j.jcat.2010.05.004.

13 J. Ng, N. Sugii, K. Kakushima, P. Ahmet, K. Tsutsui, T. Hattori and H. Iwai, *IEICE Electronic Express*, 2006, **3**, 316–321.

14 J. Liquang, S. Xiaojun, X. Baifu, W. Baiqi, C. Weimin and F. Honggang, *J. Solid State Chem.*, 2004, **177**, 3375–3382.

15 R. T. Ako, P. Ekanayake, A. L. Tan and D. J. Young, *Mater. Chem. Phys.*, 2016, **172**, 105–112.

16 Y. Liu, S. Zhou, J. Li, Y. Wang, G. Jiang, Zh. Zhao, B. Liu, X. Gong, A. Duan, J. Liu, J. Wei and L. Zhang, *Appl. Catal., B*, 2005, **168–169**, 125–131.

17 J. Zhang, Z. Zhao, X. Wang, T. Yu, J. Guan, Zh. Yu, Zh. Li and Z. Zh. Zhigang, *J. Phys. Chem. C*, 2010, **114**, 18396–18400.

18 C. B. Carter, and M. G. Norton, Sols, Gels, and Organic Chemistry, in *Ceramic Materials*, Springer, New York, NY, 2007.

19 C. T. McKee and J. Y. Walz, *J. Am. Ceram. Soc.*, 2009, **92**, 916–921.

20 S. R. Mukai, H. Nishihara, S. Shichi and H. Tamon, *Chem. Mater.*, 2004, **16**(24), 4987–4991.

21 M. Borlaf, J. M. Poveda, R. Moreno and M. T. Colomer, *J. Sol-Gel Sci. Technol.*, 2012, **63**, 408–415.

22 J. Lee and Y. Cheng, *J. Controlled Release*, 2006, **111**, 185–192.

23 S. Yuan, Q. Sheng, J. Zhang, F. Chen, M. Anpo and Q. Zhang, *Microporous Mesoporous Mater.*, 2005, **79**, 93–99.

24 S. Bakardjieva, J. Subrt, P. Pulisova, M. Marikova and L. Szatmary, *Mater. Res. Soc. Symp. Proc.*, 2011, **1352**, 129–134, DOI: 10.1557/opl.2011.1132.

25 J. Subrt, P. Pulisova, J. Bohacek, P. Bezdicka, E. Plizingrova, L. Volfova and J. Kupcik, *Mater. Res. Bull.*, 2014, **49**, 405–412.

26 E. Plizingrova, L. Volfova, P. Svora, N. Labhsetwar, M. Klementova, L. Szatmary and J. Subrt, *Catal. Today*, 2015, **240**, 107–113.

27 S. Bakardjieva, R. Fajgar, I. Jakubec, E. Koci, A. Zhigunov, E. Chatzisymeon and K. Davididou, *Catal. Today*, 2019, **328**, 189–201.

28 *JCPDS PDF-4 database*, International Centre for Diffraction Data, Newtown Square, PA, USA, release 2015.

29 B. H. Toby and R. B. Von Dreele, *J. Appl. Crystallogr.*, 2013, **46**(2), 544–549.

30 P. Scherrer, *Gottinger Nachrichle*, 1918, **2**, 98–100.

31 D. C. Palmer, *CrystalMaker*, CrystalMaker Software, Ltd, Begbroke, Oxfordshire, England, 2014.

32 J. L. Labar, *Ultramicroscopy*, 2005, **103**(3), 237–249.

33 S. Brunauer, P. H. Emmett and E. Teller, *J. Am. Chem. Soc.*, 1938, **60**, 309–319.

34 E. P. Barrett, L. G. Joyner and P. P. Halenda, *J. Am. Chem. Soc.*, 1951, **73**, 373–380.

35 J. Peral and D. Ollis, *J. Catal.*, 1992, **136**, 554–565.

36 H. Al-Ekabi and N. Serpone, *Langmuir*, 1989, **5**, 250–255.

37 J. Theurich, M. Lindner and D. W. Bahnemann, *Langmuir*, 1996, **12**, 6368–6376.

38 G. Colón, M. C. Hidalgo and J. A. Navío, *Appl. Catal., A*, 2002, **231**, 185–189.

39 M. L. Satuf, *et al.*, *Appl. Catal., B*, 2008, **82**, 37–49.

40 M. Grätzel, N. Serpone and E. Pelizzetti, *Photocatalysis, Fundamentals and Applications*, Wiley, New York, 1989.

41 S. Ghosh, A. Vasudevan, P. Rao and K. Warrier, *Br. Ceram. Trans.*, 2001, **100**, 151–154.

42 K. Li, S. Wei and W. Yang, *J. Phys. Chem. Solids*, 2011, **72**, 643–647.

43 X. Z. Ding and X. H. Liu, *J. Mater. Res.*, 1998, **13**, 2556–2559.

44 S. Sadhu and P. Poddar, *RSC Adv.*, 2013, **3**, 10363–10369.

45 Y. Xin and H. Liu, *J. Solid State Chem.*, 2001, **184**, 3240–3246.

46 B. Trujillo-Navarrete, M. del Pilar Haro-Vásquez, R. M. Félix-Navarro, F. Paraguay Delgado, H. Alvarez-Huerta, S. Pérez-Sicairos and E. A. Reynoso-Soto, *J. Rare Earths*, 2017, **35**, 259–270.

47 W. Li, A. I. Frenkel, J. C. Woicik, C. Ni and S. Ismat Shah, *Phys. Rev. B Condens. Matter Mater. Phys.*, 2005, **72**, 155315.

48 J. Liqiang, X. Xiaojin, X. Baifu, W. Baiqi, C. Weimin and F. Honggang, *J. Solid State Chem.*, 2004, **177**(10), 3375–3382.

49 D. Schwarzenbach, *Inorg. Chem.*, 1970, **9**, 2391–2397.

50 Y. B. Xie and C. W. Yuan, *Appl. Surf. Sci.*, 2004, **221**, 17–24.

51 M. Maleckova, BSc thesis, Charles University, Prague, 2014, https://is.cuni.cz/webapps/zzp/detail/160373/.

52 F. A. Kröger and H. J. Vink, *Solid State Physics*, vol. 3, Academic, New York, 1956.

53 L. Edelson and A. Glaeser, *J. Am. Ceram. Soc.*, 1988, **71**, 225–235.

54 J. Parker and R. Siegel, *J. Mater. Res.*, 1990, **5**, 1246–1252.

55 E. Plizingrova E, M. Klementova, P. Bezdicka, J. Bohacek, Z. Barbierikova, D. Dvoranova, M. Mazur, J. Krysa, J. Subrt and V. Brezova, *Catal. Today*, 2017, **281**(1), 165–180.

56 A. Gupta, *Int. J. Drug Dev. Res.*, 2012, **4**, 35–40.

57 K. Li, S. Wei and W. Yang, *J. Phys. Chem. Solids*, 2011, **72**, 643–647.

58 IUPAC, Compendium of Chem. Technol, *The Gold Book*, ed. A. D. McNaught and A. Wilkinson, 2nd edn, 2006, ISNB 0-9678550-9-8, DOI: 10.1351/goldbook.

59 R. Gopalan and Y. Lin, *Ind. Eng. Chem. Res.*, 1995, **34**, 1189–1195.

60 K. Kumar, S. Keizer and A. Burggraaf, *J. Mater. Chem.*, 1993, **3**, 917–922.

61 Z. Wang, J. Chen and X. Hu, *Mater. Lett.*, 2000, **43**, 87–90.

62 M. Ayers and A. Hunt, *Mater. Lett.*, 1998, **34**, 290–293.

63 A. M. Burgos and M. Langlet, *Thin Solid Films*, 1999, **349**, 19–23.

64 S. Yuan, Q. Sheng, J. Zhang, F. Chen, M. Anpo and Q. Zhang, *Microporous Mesoporous Mater.*, 2005, **79**, 93–99.

65 M. C. Biesinger, L. W. M. Lau, A. R. Gerson and R. S. C. Smart, *Appl. Surf. Sci.*, 2010, **257**, 887–898.

66 M. Falkowski, Ch. Kunneth, R. Materlik and A. Kersch, *npj Comput. Mater.*, 2018, **73**, 1–9.

67 B. Reddy, B. Chowdhury and P. Smirniotis, *Appl. Catal., A*, 2001, **219**, 53–60.

68 S. Anandan, Y. Ikuma and V. Murugesan, *Int. J. Photoenergy*, 2012, 921412, DOI: 10.1155/2012/921412.

69 S. M. Owen, *A Guide to Modern Inorganic Chemistry*, Willey, New York, 1991, ISBN 05820643920470216948.

70 H. Kato, K. Asakura and A. Kudo, *J. Am. Chem. Soc.*, 2003, **125**, 3082–3089.

71 R. Terzian, N. Serpone and M. A. Fox, *J. Photochem. Photobiol., A*, 1995, **90**(2–3), 125–135.

72 S. Anandan, *et al.*, *J. Mol. Catal. A: Chem.*, 2007, **266**, 2149–2157.

73 D. L. Rabenstein, *Anal. Chem.*, 1971, **43**, 1599–1605.

74 A. Maldotti, A. Molinari and R. Amadelli, *Chem. Rev.*, 2002, **102**, 3811–3820.

75 B. Ohtani, O. O. Prieto-Mahaney, D. Li and R. Abe, *J. Photochem. Photobiol., A*, 2010, **216**, 179–182.

76 A. Tiwari and L. Uzun, *Advanced Functional Materials*, ed. A. Tiwari and L. Uzun, Wiley, 2015.

77 D. C. Hurum, A. G. Agrios, K. A. Gray, T. Rajh and M. C. Thurnauer, *J. Phys. Chem. B*, 2003, **107**, 4545–4549.

78 R. Morris, J. Owen and A. Cheetham, *J. Phys. Chem. Solids*, 1995, **56**, 1297–1303.

79 I. McCulloch, M. Heeney, C. Bailey, K. Genevicius, I. McDonald, M. Shkunov, D. Sparrowe, S. Tiemey, R. Wagner, W. Zhang, M. L. Chabinyc, R. J. Kline,

M. D. McGehee and M. F. Toney, *Nat. Mater.*, 2006, **5**, 328–333.

80 Y. Liu, S. Zhou, J. Li, Y. Wang, G. Jiang, Zh. Zhao, B. Liu, X. Gong, A. Duan, J. Liu, J. Wei and L. Zhang, *Appl. Catal., B*, 2005, **168–169**, 125–131.

81 N. Rajeswari Yogamalar and A. Chandra Bose, *Appl. Phys.*, 2011, **103**, 33–42.

82 C. Wang, R. Pagel, J. K. Dohrmann and D. W. Bahnemann, *C. R. Chim.*, 2006, **9**, 761–773.

83 Z. Ma, Y. Li, Y. Lv, R. Sa, Q. Li and K. Wu, *ACS Appl. Mater. Interfaces*, 2018, **10**, 39327–39335.